J Mater Sci **(2021) 56:7434–7450**

Composites & nanocomposites

Facile synthesis of silver decorated reduced graphene oxide@zinc oxide as ternary nanocomposite: an efficient photocatalyst for the enhanced degradation of organic dye under UV–visible light

Asim Jilani[1,2,3,*], Syed Zajif Hussain[4,*], Mohammad Omaish Ansari[1,5,*], Rajeev Kumar[6],
Mohsin Raza Dustgeer[7], Mohd Hafiz Dzarfan Othman[2,3], M. A. Barakat[6], and
Ammar A. Melaibari[1]

[1] *Center of Nanotechnology, King Abdulaziz University, Jeddah 21589, Saudi Arabia*
[2] *Advanced Membrane Technology Research Centre, Universiti Teknologi Malaysia, UTM Johor Bahru, 81310 Johor, Malaysia*
[3] *Faculty of Engineering, School of Chemical and Energy Engineering, Universiti Teknologi Malaysia, UTM Johor Bahru, 81310 Johor, Malaysia*
[4] *Department of Chemistry and Chemical Engineering, SBA School of Science and Engineering (SBASSE), Lahore University of Management Sciences (LUMS), Lahore 54792, Pakistan*
[5] *School of Chemical Engineering, Yeungnam University, Gyeongsan-si, Gyeongbuk 712-749, South Korea*
[6] *Department of Environmental Sciences, Faculty of Meteorology, Environment and Arid Land Agriculture, King Abdul-Aziz University, Jeddah 21589, Saudi Arabia*
[7] *Department of Environmental Sciences and Engineering, Government College University Faisalabad, Faisalabad 38000, Pakistan*

Received: 22 August 2020
Accepted: 4 January 2021

ABSTRACT

Ternary combination of metal and metal oxide with reduced graphene oxide could be a novel potential photocatalyst towards highly efficient degradation of organic dyes under solar radiation. Herein, the novel ternary nanocomposite of silver nanoparticles with reduced graphene oxide and zinc oxide nanorods (Ag-rGO@ZnO_{NR}) were synthesized via *in situ* homogeneous coating of silver nanoparticles (Ag NPs) onto pre-assembled thermally reduced graphene oxide (rGO) encapsulated ZnO nanorods (ZnO_{NR}). The nanocomposite showed excellent aptitude towards the photodegradation of 2-chlorophenol (2-CP) under solar light irradiation. The Ag-rGO@ZnO_{NR} nanocomposite showed excellent UV–visible light harvesting due to the engineered reduced bandgap, and the Schottky barrier at the metal–semiconductor interface is expected to promote charge separation as also revealed by the optical calculations. The production of superoxide anions $^{\cdot}O_2^-$ and hydroxyl radicals ($^{\cdot}OH$) acting as substantial reducing and oxidizing agents and further $\pi - \pi$ stacking interactions with the aromatic ring of 2-CP provided an ultimate foundation for its

Handling Editor: Chris Cornelius.

Address correspondence to E-mail: asim.jilane@gmail.com; syed.hussain@lums.edu.pk; omaishchem@gmail.com

Springer

https://doi.org/10.1007/s10853-021-05783-8

100% degradation. The photocatalyst showed high reproducibility, and 94% efficiency was observed even after three cycles. XPS chemical state analysis of C1s, O1s, Zn2p, and Ag3d confirm the variation of C =C (sp^2), C–O, O= C–OH, and localization of Ag nanoparticles with rGO by confiscating the oxygen-comprising functional moieties which may be the possible reason for the enhanced photodegradation.

Introduction

An increase in the use of various organic dyes with rapid industrialization and their direct or unintentional discharge into water bodies poses a serious threat to the ecosystem. Among different contaminants, the chlorophenols or their derivatives are widely discharged as they are major constituents in industrial waste, pesticides, and insecticides, etc. and cause histopathological disorders and carcinogenic effects in human beings [1, 2]. Thus, due to this deleterious impact on human health and the ecosystem, its removal from wastewater is of utmost importance. For this, several physical or chemical techniques like oxidation, flocculation, absorption, and photocatalysis are generally employed [3]. Among these, photocatalysis is prominent in terms of its: ease of handling, high reusability of catalyst, and excellent efficiency towards the degradation of organic pollutants [4]. It is inferred that the notable performance of a photocatalytic system for dye-degradation depends upon the right selection of material and in literature, several materials such as ZnO, TiO_2, $BiVO_4$, CuO, and Fe_2O_3 have been predominantly reported [5–10]. Amongst these, ZnO has numerous advantages due to its high chemical stability, low cost, ease of synthesis, environment-friendly properties, and tunable bandgap[11] which makes it suitable for advance application in various fields such as solar cell, adsorption, sensing, etc. [12–15].

The properties of ZnO can be further enhanced by fabricating it with other metals or carbon-based materials [16]. Among various carbon-based material, reduced graphene oxide (rGO) is a highly efficient material for photocatalytic applications due to its high specific surface area, zero bandgap, and the ability to accelerate charge carrier from valance to conduction band [17]. Moreover, the ratio of sp2/sp3 bonding, high surface defects, and the ability to slow down charge recombination makes it a prominent photocatalyst in comparison to graphene oxide. The presence of π–π bonding in rGO-based photocatalytic materials also imparts additional functional sites for interaction with other metals, pollutants, etc. [18, 19].

Xue et al. [20] and other researchers [21] have reported high photocatalytic activity of rGO@ZnO based composites. However, it can be inferred that photocatalysis is highly dependent on the conductive and light-harvesting properties of the photocatalyst [22]. The addition of noble materials such as Ag, Au, etc. is expected to enhance the conductivity due to the additional or synergistic effect as well as the light-harvesting property due to the surface plasmon resonance (SPR) effect [23]. Moreover, the oxidation ability of Ag to oxidize pollutant molecules under visible and ultraviolet light also makes it an attractive dopant in ternary photocatalytic composites [24].

In contrast to the previous reports, of Ag- and rGO-based composites of ZnO [25–28], the synthesis Ag-rGO@ZnO_{NR} through facile *in situ* reduction of GO and $AgNO_3$ has been reported here. The method is advantageous as surface coating with GO, and then its reduction imparts strong interaction between ZnO_{NR} and rGO. In addition to developing the above synthetic protocol, we also calculated the variation of cell volume and texture coefficient with respect to grain size and dislocation density. Moreover, concise interaction of detected functional groups, , *that is*, C=C (sp^2), C–O, O=C–OH, Ag–O, Ag, Ag–OH, O^{2-}, OH, and their effect on the enhanced photocatalytic performance was also unveiled which is still very rare reported for Ag-rGO@ZnO_{NR}.

Experimental details

Materials

Graphite (99.99%), zinc acetate (99.99%), sulphuric acid (99.999%), silver nitrate (99%), sodium borohydride, (98%), phosphoric acid (85%), 2-CP (99%), and potassium permanganate (99%) were all purchased from Sigma-Aldrich and were used as received.

Synthesis process

The Ag-rGO@ZnO$_{NR}$ nanocomposite was prepared via a chemical route. Graphene oxide was prepared by modified Hummer's method according to our previous report, and a stock solution of 4 mg/mL was prepared by diluting it with deionized water [29]. ZnO$_{NR}$ was prepared by the combustion of zinc acetate. For this, 2 gm of zinc acetate was dissolved in 50 mL of ethanol under continuous stirring for 24 h, and subsequently, the solution was filtered, and the resulted residue was heated at 400 °C in a muffle furnace for 1 h to get ZnO$_{NR}$. For the coating of GO on ZnO$_{NR}$, 400 mg of ZnO$_{NR}$ were added to 30 mL of GO solution under stirring for 2 h. Thus, the dispersion was filtered out and subsequently subjected to heating at 400 °C for 1 h to get rGO@ZnO$_{NR}$. Lastly, the silver nanoparticles (Ag NPs) were deposited on rGO@ZnO$_{NR}$ by dispersing 315 mg of rGO@ZnO$_{NR}$ into 50 mL of 21 mM aqueous solution of $AgNO_3$ under stirring for 10 min followed by dropwise slow addition of 20 mL of 105 mM freshly prepared solution of $NaBH_4$. Thus, prepared Ag-rGO@ZnO$_{NR}$ were filtered, washed with an excess of water and ethanol, and finally dried at 50 °C for 2 h. Figure 1 illustrates the schematic synthesis process for Ag-rGO@ZnO$_{NR}$.

Photocatalytic experiment

The photocatalytic properties of ZnO$_{NR}$, rGO@ZnO$_{NR}$, and Ag-rGO@ZnO$_{NR}$ were investigated by mixing 20 mg of each into 100 mL of 50 ppm solution of 2-CP. The dispersion was initially placed in the dark for 60 min in order to attain the absorption equilibrium, and then photocatalysis was done under solar-simulated light for 120 min. The solutions were irradiated with solar light, and after every 30 min, 2.5 mL of each solution was taken out with the help of pipette for further analysis. The remaining concentration of 2-CP was analysed using HACH-DR6000, UV–visible spectrophotometer.

Characterizations

The structural analysis was done by X-ray diffraction (Rigv aku Ultima-IV) and X-ray photoelectron spectroscopy (VersaPobeII) to study the surface chemical interactions, while the morphological studies were done by SEM (JEOL—JSM7600 F) and TEM (JEOL). The properties of charge recombination ratios were studied by photoluminescence measurements using Shimadzu RF-5301PC, spectro-fluorophotometer, and the excitation wavelength for PL analysis was 325 nm for all samples. The absorbance spectra were recorded by diffuse reflectance spectrophotometer (HACH LANGE DR 6000).

Results and discussion

Structural analysis

The diffraction pattern of ZnO$_{NR}$, rGO@ZnO$_{NR}$, and Ag-rGO@ZnO$_{NR}$ (Fig. 2) reveals the crystalline nature of the prepared samples. The ZnO$_{NR}$ shows the main diffraction peak along (101) plane, followed by several other diffraction planes at (100), (002), (102), (110), (103), (200), (112), and (201) which is attributed to the zincite structure of ZnO$_{NR}$ (JCPD # 01-073-8765). The diffraction pattern of rGO@ZnO$_{NR}$ is similar to that of ZnO$_{NR}$. However, the *d*-spacing of (101) increased from 0.21 to 0.24 Å, which can be attributed to the lattice defects among the layers of rGO sheets [30]. Further, the absence of a diffraction peak for rGO was noticed in rGO@ZnO$_{NR}$. The rGO has a non-observed diffraction peak of graphite, which associates the minimal functional groups attached to the basal plane of the grapheme [31]. The diffraction pattern of Ag-rGO@ZnO$_{NR}$ indicates the presence of an additional diffraction peak in comparison to ZnO$_{NR}$ and rGO@ZnO$_{NR}$. The other diffraction peaks confirm the existence of Ag and are attributed to the (111), (200), and (220) planes at $2\theta = 38.16°$, $44.35°$, and $2\theta = 64.45°$, respectively (JCPD # 00-001-1167). However, the incorporation of Ag increases the grain size of the main diffraction peak (101) of ZnO$_{NR}$ from 33.76 to 34.52 nm. This grain size increment is caused by the difference of ionic charge among Zn and Ag and amphoteric dopant nature of Ag, which supports the crystal growth in Ag-rGO@ZnO$_{NR}$ [32]. In summary, the lattice planes of ZnO$_{NR}$ have remained the same in

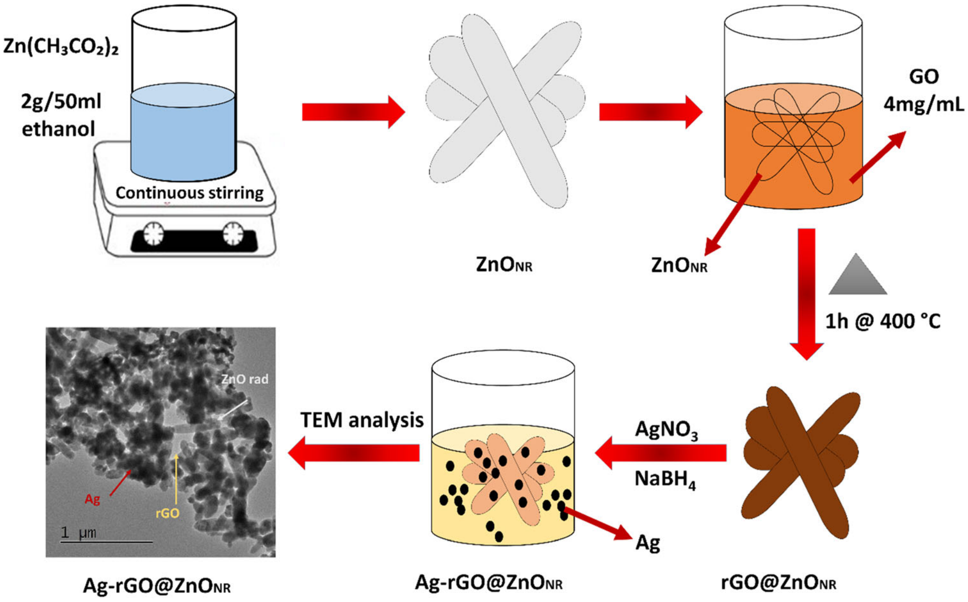

Figure 1 Schematic representation for the synthesis of Ag-rGO@ZnO_{NR} through facile in situ reduction of graphene oxide (GO) and silver precursor ($AgNO_3$).

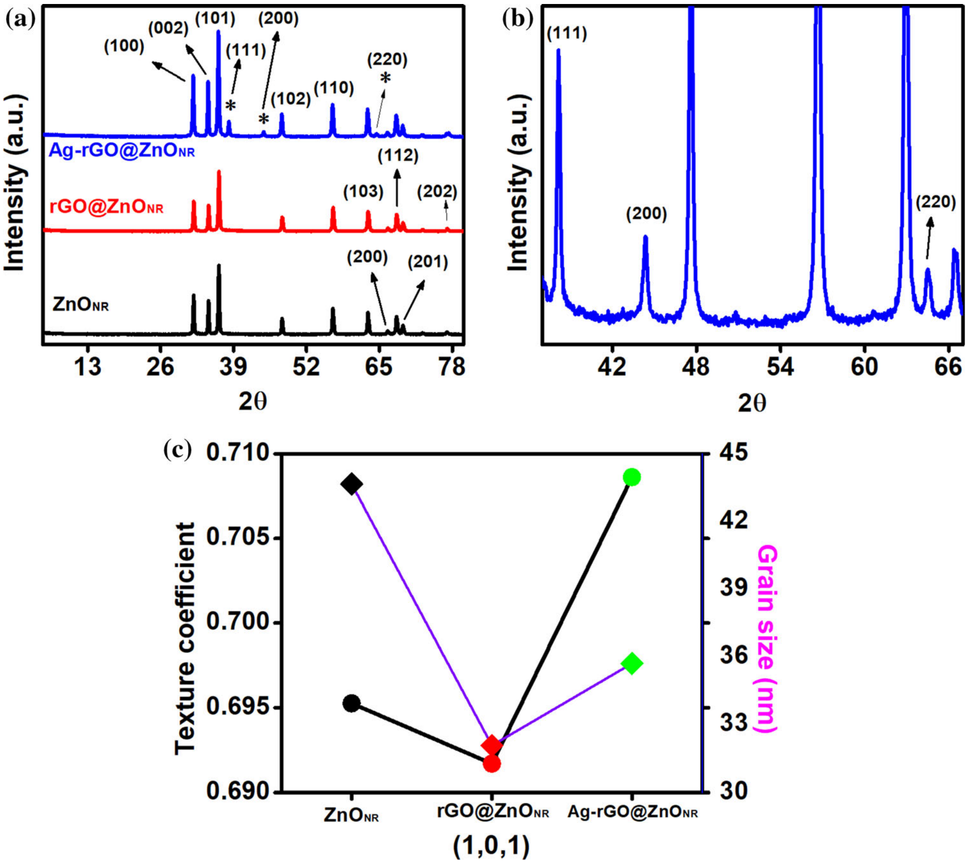

Figure 2 **a** Diffraction pattern of ZnO_{NR}, rGO@ZnO_{NR}, and Ag-rGO@ZnO_{NR}, where * indicates the presences of Ag, (**b**) diffraction pattern $2\theta = 40°–67°$ of Ag-rGO@ZnO_{NR}, (**c**) Texture coefficient of (101) and grain size.

rGO@ZnO_{NR} and Ag-rGO@ZnO_{NR}. The average grain size of ZnO_{NR}, rGO@ZnO_{NR}, and Ag-rGO@ZnO_{NR} can be estimated by the Scherrer equation

$$D = \frac{K\lambda}{\beta \cos\theta} \quad (1)$$

In the above equation, D is the estimated crystalline size of diffraction planes, β is the corresponding full-width half maximum of diffraction planes, k is constant while λ is the wavelength. The average grain size of ZnO_{NR} was calculated to be 43.65 nm. However, in the case of rGO@ZnO_{NR}, the grain size dropped to 32.07 nm. The reduction of grain size can be attributed to the constrain grain boundary migration effect, which restricts the growth of grains, as reported by Basu et al. [33].

The grain size of Ag-rGO@ZnO_{NR} showed a slight increase in comparison with rGO@ZnO_{NR} and was calculated to be 35.72 nm. This increment upon Ag doping shows that Ag has occupied the interstitial sites of rGO@ZnO_{NR} [34]. The presence of Ag and rGO can further alter the dislocation into ZnO_{NR} crystal, which was calculated by the following relation [35].

$$\delta = \frac{1}{D^2} \tag{2}$$

where D is the grain size calculated through Scherrer equation, the dislocation density of ZnO_{NR} was calculated to be 5.48×10^{-4} nm, while for rGO@ZnO_{NR} and Ag-rGO@ZnO_{NR}, it was 7.11×10^{-3} and 8.14×10^{-4} nm, respectively. The variation in dislocation density can further affect the lattice strain of the material. The lattice strain of ZnO_{NR}, rGO@ZnO_{NR}, and Ag-rGO@ZnO_{NR} was calculated by the following equation [36]:

$$\varepsilon = \frac{\beta \cos\theta}{4} \tag{3}$$

where θ is the diffraction angle while β is the full-width half maximum of the diffraction peaks. The lattice strain of ZnO_{NR}, rGO@ZnO_{NR} and Ag-rGO@ZnO_{NR} was calculated to be 8.06×10^{-4}, 1.70×10^{-3} and 9.08×10^{-4} nm, respectively. There is a possibility that Ag atom occupies interstitial space in rGO@ZnO_{NR} without much deformation in the structure. This interstitial occupied atoms or ions significantly contribute to the stability of Ag-rGO@ZnO_{NR}, which as results reduce the lattice strain and dislocation of Ag-rGO@ZnO_{NR} in comparison to rGO@ZnO_{NR} [37]. The presence of functional groups such as hydroxide and carbonyl of rGO can also alter unit cell volume of ZnO_{NR}. Moreover, Ag nanoparticles can also affect the interaction between ZnO_{NR} and rGO that ultimately varies the photocatalytic activity. Therefore, the unit cell volume of ZnO_{NR}, rGO@ZnO_{NR}, and Ag-rGO@ZnO_{NR} was calculated by the following relation [38]:

$$V = \frac{\sqrt{3}(a^2)}{2} \tag{4}$$

The unit cell volume was calculated to be 4.72, 4.74, and 4.76 nm for ZnO_{NR}, rGO@ZnO_{NR}, and Ag-rGO@ZnO_{NR}, respectively. Further, the diffraction pattern shows the presence of the most intense diffraction plane along (101); therefore, texture coefficient of (101) was calculated for the possible variation due to rGO and Ag nanoparticles by [39]:

$$TC_{hkl} = \frac{I_{hkl}/Io_{hkl}}{(1/n)\sum I_{hkl}/Io_{hkl}} \tag{5}$$

where, I_{hkl} is the intensity of the lattice planes (101) of ZnO_{NR}, while Io_{hkl} is the reference intensity of (101) plane as reported in JCPD # 01-073-8765 while n is total diffraction planes for ZnO_{NR}, rGO@ZnO_{NR}, and Ag-rGO@ZnO_{NR}. Table 1 lists the complete structural parameters of ZnO_{NR}, rGO@ZnO_{NR}, and Ag-rGO@ZnO_{NR}. Therefore, in conclusion, diffraction analysis revealed the occupation of interstitial sites of rGO@ZnO by Ag, which as a result alter the grain size, dislocation density, cell volume, and texture coefficient.

Morphological analysis

The surface morphology of ZnO_{NR} (Fig. 3a) showed the presence of rods with length in the range of ~ 200–700 nm. The variation in length might be due to the breaking of rods during genesis or its annealing. In the case of rGO@ZnO_{NR} (Fig. 3b), the ZnO_{NR} attached or partially embedded on the surface of rGO sheets can be seen. The ZnO_{NR} in rGO@ZnO_{NR} seems to be of a much smaller size than of ZnO_{NR} prepared alone. It can be interpreted that GO-coated ZnO_{NR} on high-temperature heating during the reduction process imparts strain on ZnO_{NR}, thereby resulting in the breaking of some ZnO_{NR}. The rGO coated as well as partially or wholly embedded ZnO_{NR} inside rGO sheets is expected to provide an easy pathway for the transport of charge carriers, which is highly desirable for the efficient photocatalytic process [40]. The surface analysis of Ag-rGO@ZnO_{NR} (Fig. 3c) shows the slight breaking of rGO sheets apart from the embedded ZnO_{NR}, which can be attributed to the strong interaction among the Ag nanoparticle, rGO, and ZnO_{NR} [41]. This breaking of rGO sheets results in some surface defects that could be useful to trap pollutants during the photodegradation process [29].

Table 1 Calculated crystalline parameters through diffraction pattern for ZnO_{NR}, rGO@ZnO_{NR}, and Ag-rGO@ZnO_{NR}

Sample details	Crystalline parameters				
	Grain size (nm)	Dislocation density (nm)	Lattice strain (nm)	Texture coefficient(1,0,1)	V_{cell} (nm)
ZnO_{NR}	43.65	5.48×10^{-4}	8.06×10^{-4}	0.68	4.72
rGO@ZnO_{NR}	32.07	7.11×10^{-3}	1.70×10^{-3}	0.69	4.74
Ag-rGO@ZnO_{NR}	35.72	8.14×10^{-4}	9.08×10^{-4}	0.70	4.76

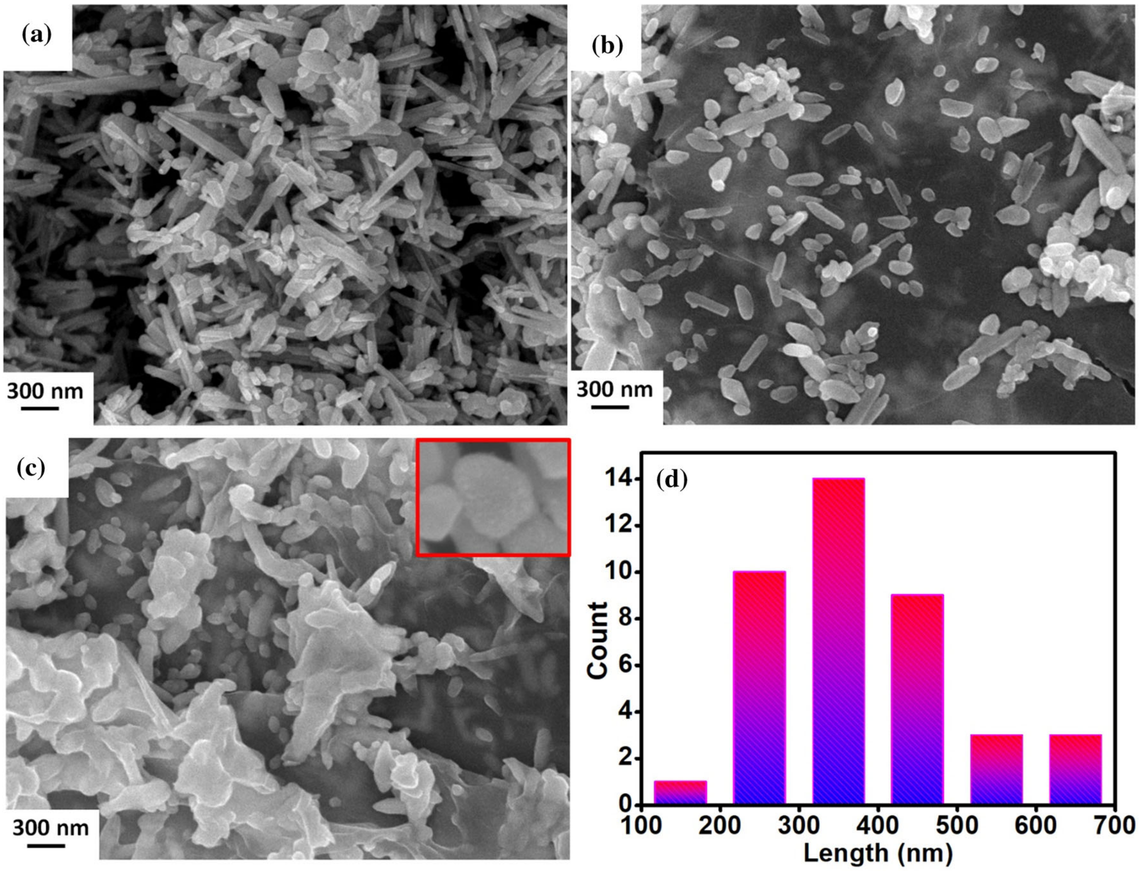

Figure 3 Field emission scanning morphology of (**a**) ZnO_{NR} (**b**) rGO@ZnO_{NR} (**c**) Ag-rGO@ZnO_{NR} and (**d**) average length of ZnO_{NR}.

The inset (Fig. 3c) at high magnification shows that Ag nanoparticles are irregular spherical in shape. However, Ag nanoparticles were small in size and could not be observed by FESEM. Therefore, TEM analysis was performed for Ag-rGO@ZnO_{NR}. The approximate calculated length of ZnO_{NR} shown in Fig. 3d. High-resolution TEM analysis of Ag-rGO@ZnO_{NR} (Fig. 4) confirms Ag nanoparticles Moreover, Ag nanoparticles were found uniformly coated over the surface of rGO@ZnO_{NR}.

Optical properties

Absorbance spectra of ZnO_{NR}, rGO@ZnO_{NR}, and Ag-rGO@ZnO_{NR} is shown in Fig. 5a. The absorbance edge of ZnO_{NR} is ~ 400 nm, while for rGO@ZnO_{NR}, the band edge shifted to longer wavelength, which indicated the absorption of more light photons by rGO [42]. In the case of Ag-rGO@ZnO_{NR} photocatalyst, band edge further shifted to longer wavelength with the observance of the small hump at ~ 440 nm, corresponding to the surface plasmon resonance of Ag nanoparticles. This surface plasmon resonance is

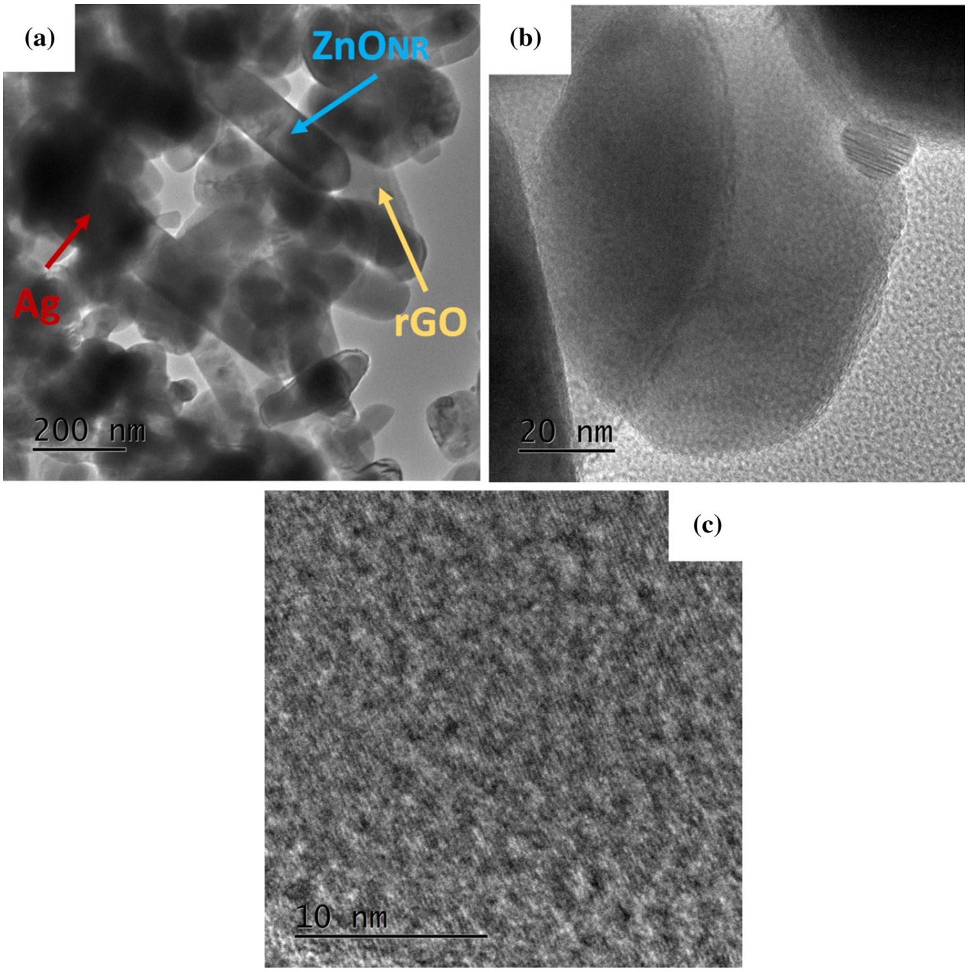

Figure 4 Low to high-resolution morphology of Ag-rGO@ZnO$_{NR}$ by transmission electron microscopy.

the fundamental properties of the Ag nanoparticles, which is attributed to the absorption and oscillation of photons with higher energy and is expected to enhance the charge carrier movement in Ag-rGO@ZnO$_{NR}$ photocatalyst. The bandgap of prepared ternary nanocomposites photocatalyst was calculated by applying Kubelka–Munk function [43].

$$F(R) = (1 - R/100)^2/2R \tag{6}$$

Here, R is the reflectance of the photocatalyst. The calculated bandgap of ZnO$_{NR}$ (Fig. 5b) was ~ 3.05 eV, which is lower than the previously reported data [44]. The lower bandgap shows its conductive nature. The bandgap of rGO@ZnO$_{NR}$ was calculated to be ~ 2.92 eV (Fig. 5c), while for Ag-rGO@ZnO$_{NR}$ photocatalyst, it came out to be 2.87 eV (Fig. 5d). The reduction in the bandgap clearly reveals the role of rGO and Ag nanoparticles to boost the movement of charge carriers 9 from valance to the conduction band of the ternary photocatalyst. In Fig. 5d, the band edge of Ag nanoparticle was estimated at around 2.42 eV. The reduction in the bandgap of ZnO$_{NR}$ photocatalyst due to the additional effect of rGO and Ag nanoparticles also affects the reduction and oxidation strength of ZnO$_{NR}$. The reduction strength or conduction band edge (E_{cb}) and oxidation power or valance band edge (E_{vb}) of ZnO$_{NR}$, rGO@ZnO$_{NR}$ and Ag-rGO@ZnO$_{NR}$ was estimated by the following relation [45].

$$E_{vb} = X - E_o + 0.5E_g \tag{7}$$

$$E_{cb} = E_{vb} - E_g \tag{8}$$

$$X = [x\,(A)^a\,x\,(B)^b\,x\,(C)^c]^{\frac{1}{(a+b+c)}} \tag{9}$$

In the above equation; X is the electronegativity of semiconductor under investigation while a, b and c are the number of atoms present in the compound [46]. The value of X for ZnO$_{NR}$ is 5.79 eV, while E_o is the energy of free-electron on hydrogen-scale, whose value is 4.5 eV [47, 48].The E_{vb} and E_{cb} of ZnO$_{NR}$

Figure 5 (**a**) Absorbance spectra (**b**, **c**) bandgap (**e**) PL spectra of ZnO_{NR}, $rGO@ZnO_{NR}$, and Ag-$rGO@ZnO_{NR}$.

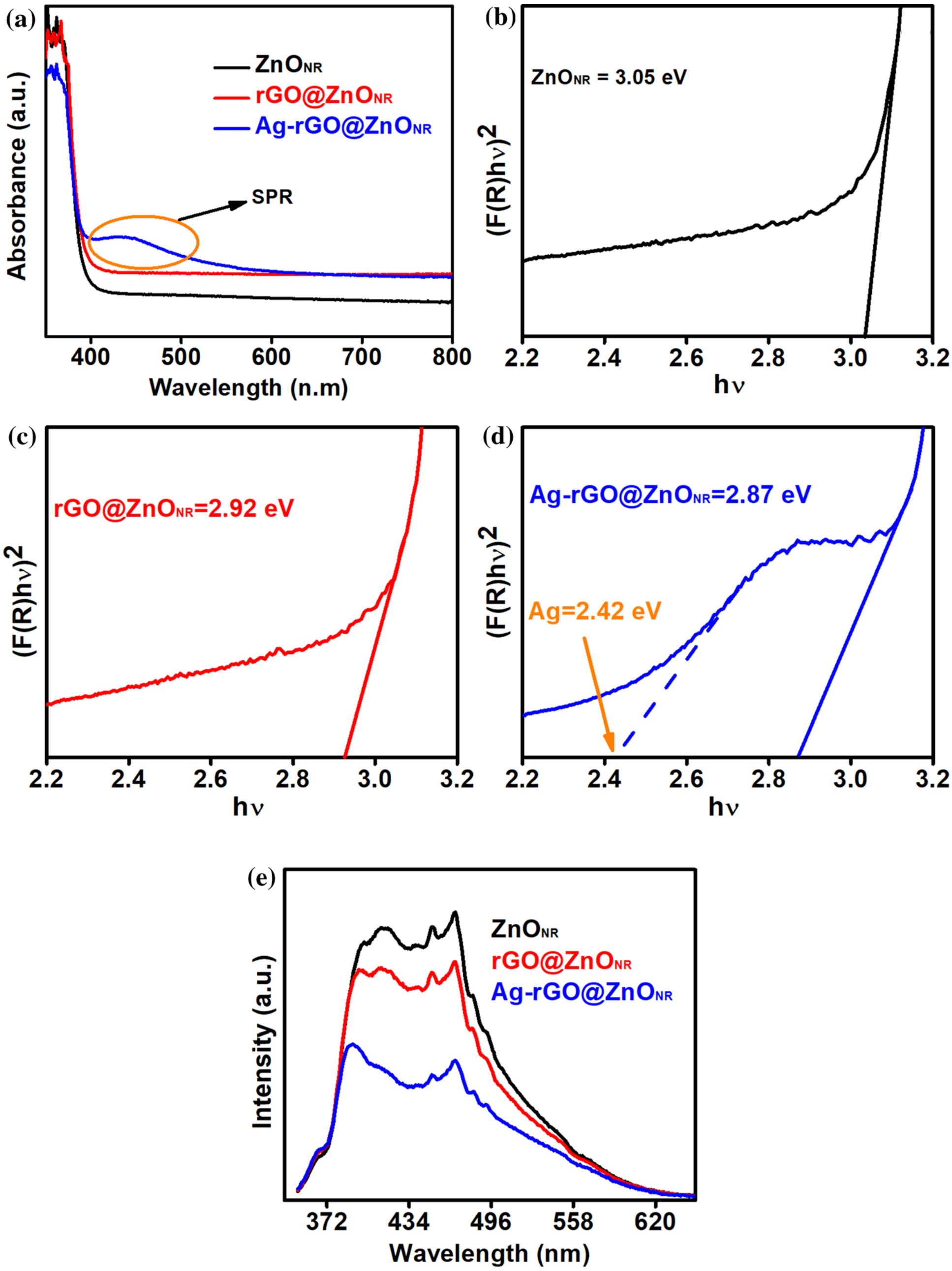

photocatalyst were calculated to be + 2.815 and − 0.235 eV, respectively. It is inferred that the oxidation power of ZnO_{NR} decreased by the addition of rGO and Ag nanoparticles while the reduction strength became more negative (Table 2).

The conduction of charge carriers from valance to conduction band may recombine, which ultimately affect the photocatalytic activity of the subjected material. The higher charge recombination will decline its photocatalytic ability. PL spectra, in this regard, provide enough information about the charge

Table 2 Values of bandgap energy, valence band, and conduction band potentials of ZnO_{NR}, $rGO@ZnO_{NR}$, and Ag-$rGO@ZnO_{NR}$ nanocomposite

Sample detail	Parameters		
	E_{vb}	E_{cb}	Bandgap (eV)
ZnO_{NR}	2.815	− 0.235	3.05
$rGO@ZnO_{NR}$	2.750	− 0.170	2.92
Ag-$rGO@ZnO_{NR}$	2.725	− 0.145	2.87

recombination ratios (Fig. 5e). Moreover, PL intensity also depends on various factors such as variation in grain size, the diameter of ZnO_{NR} and further their interface as reported by Kim et al. [49] which is also consistent with our analysis (Sect. 3.1). In the case of ZnO_{NR} photocatalyst, the appearance of two main PL bands at ~ 417 and 469 nm is attributed to the blue and green emission, respectively [50]. The blue emission corresponds to the recombination of excitons from conduction to valance band while the green emission relates to the defects that could be due to zinc, oxygen interstitials, and vacancies [51]. However, the surface defects of the ZnO_{NR} are evident from green emission. Moreover, the intensity of PL spectra directly linked to the charge recombination ratio and the decrease in PL intensity with the addition of rGO and Ag in ZnO_{NR} suggests a decline in the charge recombination ratio. Moreover, in comparison to ZnO_{NR}, the PL peaks shifted for rGO@ZnO_{NR}, which is due to the possible interaction among the functional groups such as carbonyl, epoxide of rGO and ZnO_{NR} interstitials. Moreover, this interaction may lead to some surface defects that could provide attractive sites for the absorption of pollutants. Furthermore, Ag-rGO@ZnO_{NR} shows the border of the PL emission peak, which is attributed to the variation in surface defects [52]. Moreover, the intensity of PL also attributed to shallow and deep defects. The deep defects are directly linked to the enhancement in the charge recombination ratio of the subjected material while shallow defects represent the decline in charge recombination ratio as reported by Choudhury et al. [53]. Here, the PL results (Fig. 5e) shows the decrement in the PL intensity for Ag-rGO@ZnO_{NR} which also confirm the increment in shallow defects that is highly desirable for the enhancement in the photocatalytic activity [53].

Chemical state interaction

The surface composition of ZnO_{NR}, rGO@ZnO_{NR} and Ag- rGO@ZnO_{NR} was analysed by the XPS (Fig. 6a), which suggests the presence of Zn2p, and O1s for ZnO_{NR}; Zn2p, O1s, and C1s for rGO@ZnO_{NR}. Moreover, the appearance of Ag3p3 and Ag3d in the case of Ag-rGO@ZnO_{NR} along with Zn2p, O1s, and C1s also confirmed the successful incorporation of Ag in rGO@ZnO_{NR} and the efficacy of the preparation technique. The atomic percentage for each detected element is shown in Fig. 6b.

High-resolution C1s spectra of rGO@ZnO_{NR} and Ag-rGO@ZnO_{NR} (Fig. 7 a and b) show the appearances of peak positions at around 284.6 eV, 285.7, and 286.6 eV which attributed, respectively, to C=C (sp^2), C–O and O=C–OH functional groups of rGO [54, 55]. These functional groups provide an attractive site for interaction of rGO with ZnO_{NR} and Ag, which further leads to varies the application of rGO-based composites [56]. The total contribution of C=C was 50.44%, while that of C–O and O=C–OH were found around 44.25 and 5.31%, respectively, for rGO@ZnO_{NR} (Fig. 7a). However, after the introduction of Ag variation in C=C (sp^2), C–O and O=C–OH were noticed. So, in the case of Ag-rGO@ZnO_{NR} (Fig. 7b), C=C (sp^2), C-O, and O=C–OH was around 91.57%, 4.07 and 4.36%, respectively. These results indicated the reduction of O=C–OH from 44.25 to 4.07% while incrementing of C=C (sp^2) from 50.44 to 91.57%. The oxygen-comprising functional moieties of rGO facilitate the Ag nanoparticles to form the binding with rGO that ultimately rescued the oxygen functional groups in Ag-rGO@ZnO_{NR}. These findings are consistent with the report on the interaction of Ag and rGO, which experimentally proved the localization of Ag nanoparticles with rGO by confiscating the oxygen-based functional groups [57]. Total variation of C=C (sp^2), C–O, and O=C–OH for rGO@ZnO_{NR} and Ag-rGO@ZnO_{NR} are shown in Fig. 7c.

Chemical state of Ag 3d5/2 for Ag-rGO@ZnO_{NR} shows (Fig. 7d) interaction of silver with oxygen and hydroxide functional groups of ZnO_{NR} and rGO. Three peaks around 367.05 eV, 368.04, and 369.28 eV that attributed to Ag–O, Ag, and Ag–OH, respectively [58]. Contribution of Ag was about 90.37%, while some fraction of functional groups from rGO and ZnO_{NR} leads to the formation of Ag–O (5.36%) and Ag–OH (4.28%).

Zn2p3 analysis of ZnO_{NR} (Fig. 8a) shows the presence of two peaks around 1021.84 eV and 1022.92 eV attributed to Zn (60.07%) and chemisorbed oxygen, that is, Oi (39.93%) [58]. However, with the introduction of rGO (in case of rGO@ZnO_{NR}), the contribution of Oi increased from 39.93 to 46.0% while ZnO_{NR} decreased from 60.07 to 54.00% (Fig. 8b). The different functional groups of rGO may interact with ZnO_{NR} that results in non-stoichiometric ZnO_{NR}, and thus the change in the contribution of Oi and ZnO_{NR} was observed [59]. Moreover, the separation binding energy changed from 1.08 to 1.18 eV. All these changes also affirm the

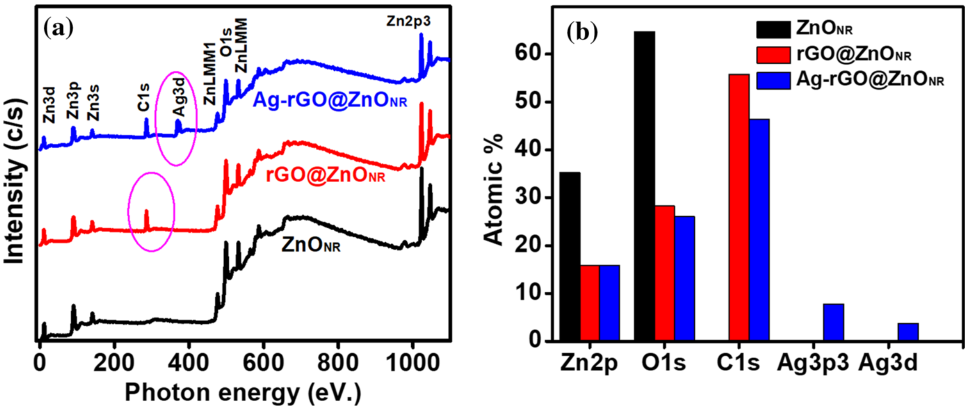

Figure 6 XPS survey scans (**a**) and (**b**) composition analysis of ZnO_{NR}, $rGO@ZnO_{NR}$,, and Ag-$rGO@ZnO_{NR}$.

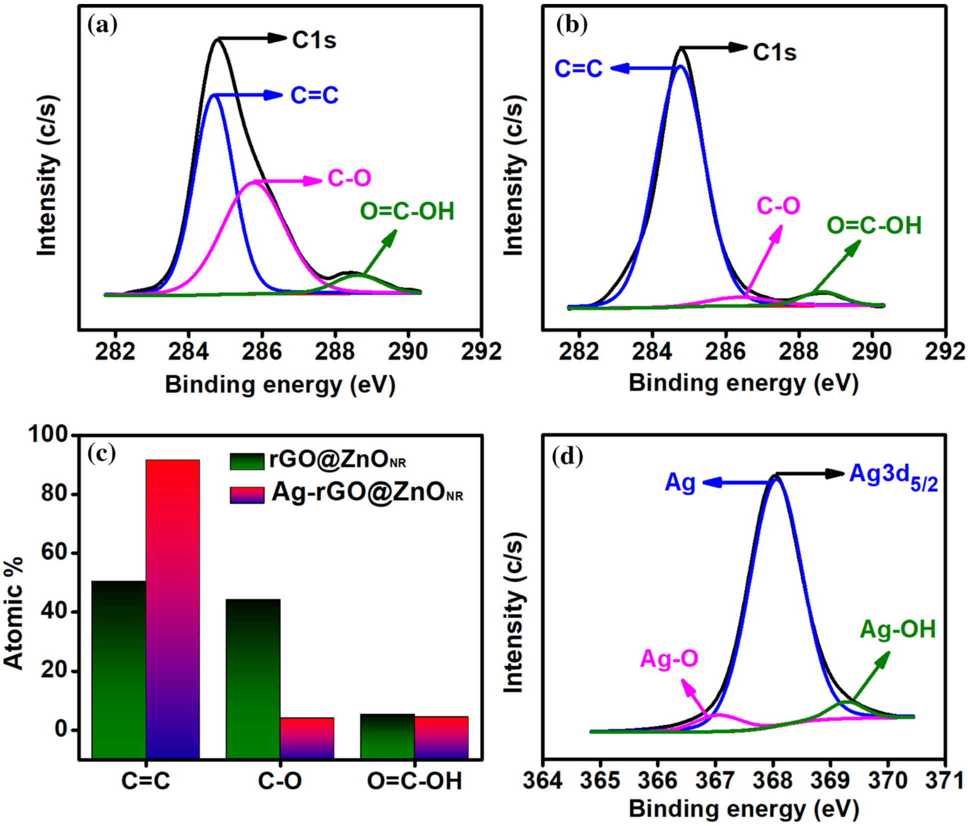

Figure 7 C1s spectra of (**a**) $rGO@ZnO_{NR}$, (**b**) Ag-$rGO@ZnO_{NR}$, (**c**) total variation of functional groups and (**d**) Ag 3d5/2 of Ag-$rGO@ZnO_{NR}$.

interaction of ZnO_{NR} and rGO. Further, in the case of Ag-$rGO@ZnO_{NR}$ (Fig. 8c) contribution of Zn increased to 77.76% while Ag nanoparticles also affected the interaction along with rGO.

O1s spectra of ZnO_{NR} (Fig. 9a) shows the presence of peaks at around 531, 532.7, and 534.3 eV, corresponding to oxygen radicals(O^{2-}), hydroxide (OH) and some fraction bridging oxygen (O_{Brg}), respectively [58, 60, 61]. The contribution of O^{2-} (59.51%) is highest, followed by OH (29.85%) and O_{Brg} (10.65%). However, after the addition of rGO, the contribution of O^{2-} decreased (51.17%) while that of OH and O_{Brg} increased to 34.92 and 13.91%, respectively (Fig. 9b). This can be attributed to the various functional groups present at the basal planes of rGO indicating the interactions among ZnO_{NR} and rGO [62]. Moreover, the O_{Brg} contribution reduced to 2.07% in the case of Ag-$rGO@ZnO_{NR}$ which indicates the role of O_{Brg} by providing attractive sites to Ag through the diffusion of oxygen vacancies and also results in the reduction of OH from 34.92 to 28.47% (Fig. 9c) [63]. The total variation of O^{2-}, OH, and O_{Brg} for ZnO_{NR},

Figure 8 Zn2p3 analysis of (**a**) ZnO_{NR} (**b**) rGO@ZnO_{NR}, and (**c**) Ag-rGO@ZnO_{NR}.

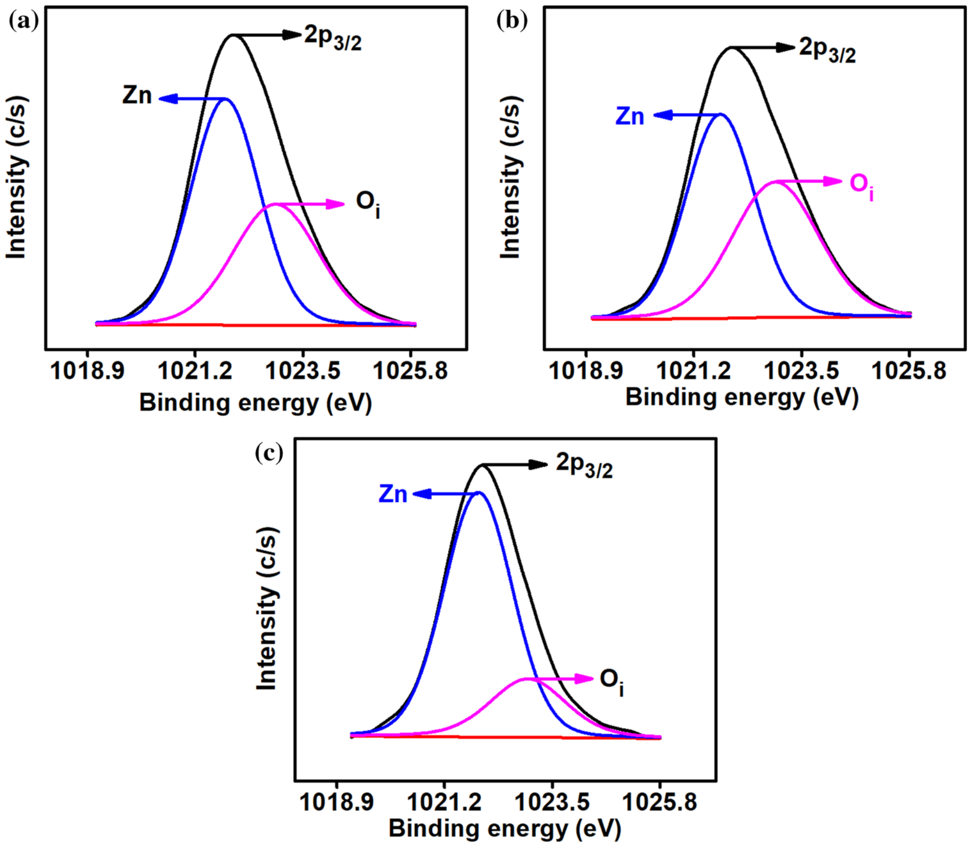

rGO@$ZnO_{NR,}$ and Ag-rGO@ZnO_{NR} is presented in Fig. 9d.

Photocatalysis degradation of 2-CP

The adsorption, photolysis, and photocatalysis of 2-CP onto ZnO_{NR}, rGO@$ZnO_{NR,}$, and Ag-rGO@ZnO_{NR} nanocomposite are shown in Fig. 10a. The adsorption of the 2-CP shows the attainment of the equilibrium within 60 min, and the adsorption was 20.2, 23.7, and 28.7%, for ZnO_{NR}, rGO@ZnO_{NR} , and Ag-rGO@ZnO_{NR}, respectively. The adsorption increases with the increase in the functionality of ZnO_{NR} hybridization with rGO and Ag, as it provides more binding sites for the interaction with 2-CP molecules. After adsorption in the dark, the 2-CP solutions were exposed to solar light, and the photocatalytic decomposition of the 2-CP was found to increase with the increase in reaction time. Ag-rGO@ZnO_{NR} nanocomposite showed better photocatalytic properties than ZnO_{NR}, rGO@ZnO_{NR} nanocomposite, as evident in Fig. 10a. The photolysis of 2-CP under solar light was 39.6% while in contrast, ZnO_{NR} showed 72% decomposition under similar experimental conditions. Although ZnO_{NR} is not a proven visible light photocatalyst, here it showed satisfactory decomposition of 2-CP. This may be explained by the fact that solar light has a little fraction of UV light, and this combination of UV and visible light (solar light) resulted in effective degradation. Moreover, the oxygen-rich surface and defects in the ZnO_{NR} crystalline structure might be responsible for the photocatalytic efficiency in solar light [64]. The UV–visible absorption band edge of ZnO_{NR} is around 400 nm (Fig. 5a), and the bandgap energy of 3.05 eV reveals that ZnO_{NR} is capable of absorbing the energy (photons) from the solar light. The photocatalytic efficacy of the rGO@ZnO_{NR} and Ag-rGO@ZnO_{NR} nanocomposite is 89 and 100%, respectively. The enhanced photocatalytic efficacy of rGO@ZnO_{NR} and Ag-rGO@ZnO_{NR} nanocomposite is mainly due to higher adsorption of photons and better separation of the photogenerated electrons and holes. Moreover, the coupling of the Ag with rGO@ZnO_{NR} augmented free exciton emissions and reduced the bound exciton emissions in Ag-rGO@ZnO_{NR} nanocomposite [65]. In the

Figure 9 O1s analysis of ZnO_{NR}, rGO@ZnO_{NR},, and Ag-rGO@ZnO_{NR}.

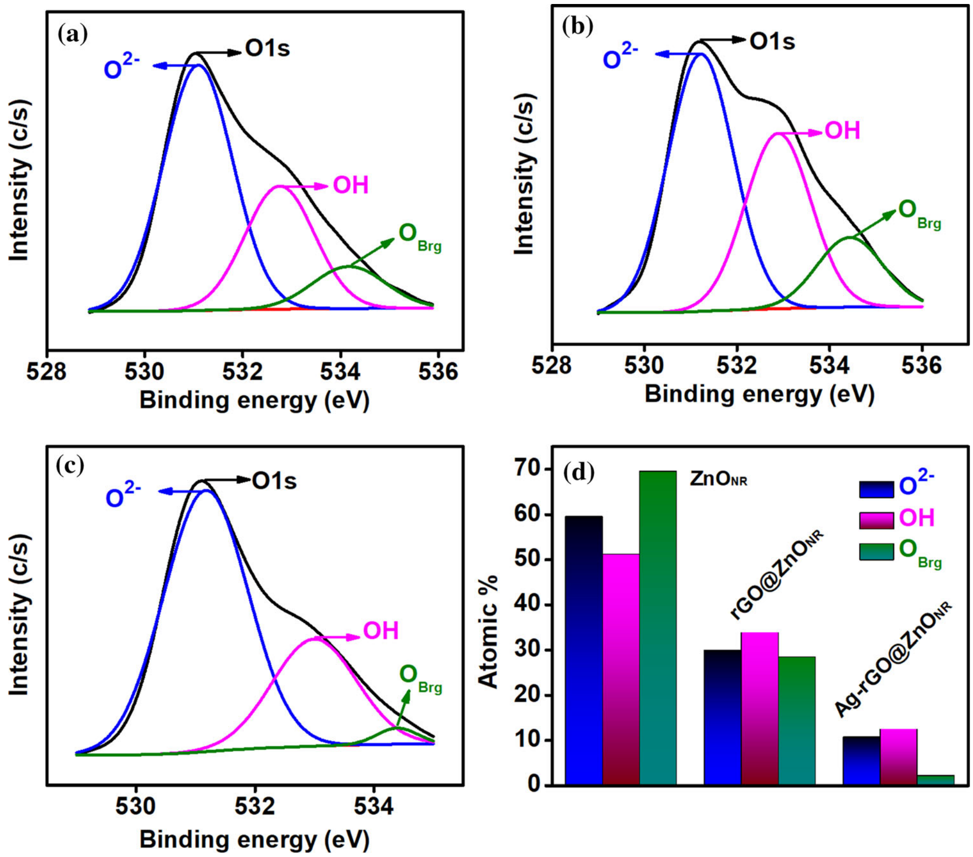

Figure 10 (**a**) Photocatalytic degradation of 2-CP by ZnO_{NR}, rGO@ZnO_{NR}, and Ag-rGO@ZnO_{NR} nanocomposite (solution volume-100 mL, pH-6.55, conc.-31 mg/L), (**b**) Plot for the first-order kinetic model for the 2-CP photodegradation onto ZnO_{NR}, rGO@ZnO_{NR} and Ag-rGO@ZnO_{NR} nanocomposite, and (**c**) The reusability of Ag-rGO@ZnO_{NR} nanocomposite for the 2-CP photocatalytic decomposition.

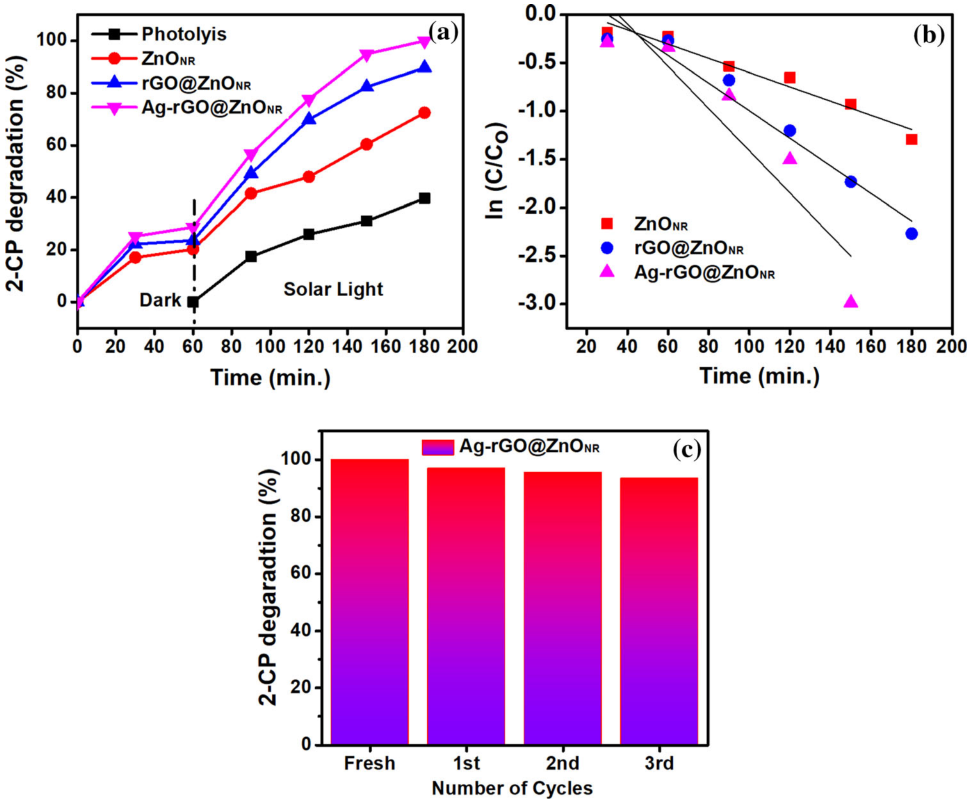

rGO@ZnO$_{NR}$ and Ag-rGO@ZnO$_{NR}$ nanocomposite, the rGO also helps to enhance the photocatalytic activity of ZnO$_{NR}$ and Ag by providing $\pi - \pi$ stacking interactions between the aromatic ring of 2-CP and the aromatic structure of rGO which accelerates the transfer of photogenerated electrons [66]. The PL analysis (Fig. 5e) clearly reveals that the recombination ratio of photogenerated e^-/h^+ reduces in the following order, that is, ZnO$_{NR}$ < rGO@ZnO$_{NR}$ < Ag-rGO@ZnO$_{NR}$. The reduction in the PL peak intensity is clear evidence of better charge separation and formation of heterojunction in Ag-rGO@ZnO$_{NR}$ after coupling the rGO and Ag with ZnO$_{NR}$ [52]. Therefore, Ag-rGO@ZnO$_{NR}$ showed better photocatalytic efficiency as compared to ZnO$_{NR}$ and rGO@ZnO$_{NR}$.

The rate of 2-CP photodegradation by ZnO$_{NR}$, rGO@ZnO$_{NR}$, and Ag-rGO@ZnO$_{NR}$ nanocomposite can be considered as the first-order kinetic model.

$$\ln(C/C_o) = -kt \tag{10}$$

where C_o and C are the initial and final concentrations (mg/L) of 2-CP after time t, respectively, k is the degradation rate constant (1/min), and its values were calculated from the plot $\ln(C/C_o)$ versus t (Fig. 10b). The values of rate constant (k) are estimated to be 7.40×10^{-3}, 14.30×10^{-3} and 21.8×10^{-3} min^{-1} for 2-CP degradation onto ZnO$_{NR}$, rGO@ZnO$_{NR}$, and Ag-rGO@ZnO$_{NR}$ nanocomposite, respectively. This indicates that Ag-rGO@ZnO$_{NR}$ nanocomposite is the most efficient catalyst amongst others for the degradation of 2-CP [67].

Degradation mechanism of 2-CP

The mechanism for higher 2-CP photocatalytic degradation onto the rGO@ZnO$_{NR}$ and Ag-rGO@ZnO$_{NR}$ nanocomposite can be explained on the basis of heterojunction formation between the ZnO$_{NR}$ and rGO. Besides the heterojunction formation, there are several factors such as experimental conditions, radiation source, catalyst grain size, etc. may have the effect of the photocatalysis process. As the XRD analysis showed, the grain size of the rGO@ZnO$_{NR}$ (32.07 nm) and Ag-rGO@ZnO$_{NR}$ (35.72 nm) is smaller than the pure ZnO$_{NR}$, which may facilities the higher photocatalysis reaction due to small size and large surface area [58]. The E_{vb} and E_{cb} of ZnO$_{NR}$ photocatalyst were calculated to be + 2.815 and − 0.235 eV, respectively, vs normal hydrogen electrode (NHE). After coupling the rGO with ZnO$_{NR}$, a shift in E_{vb} (+ 2.75 eV) and E_{cb} (− 0.17 eV) of rGO@ZnO$_{NR}$ is observed. The incorporation of Ag on rGO@ZnO$_{NR}$ showed a slight change in E_{vb} (+ 2.72 eV) while the E_{cb} showed a noticeable change (− 0.145 eV). Moreover, Ag is a noble plasmonic nanoparticle, and after coupling with rGO@ZnO$_{NR}$, absorption photons in visible range occurs due to the localized surface plasmon resonance of Ag [68]. The Ag attached to rGO@ZnO$_{NR}$ surface also forms a Schottky barrier at the interface, which helps in the efficient separation of charge carriers, thereby resulting in the enhancement of the decomposition of 2-CP by Ag-rGO@ZnO$_{NR}$ nanocomposite. A reduction in the bandgap energy and PL intensity of the Ag-rGO@ZnO$_{NR}$ nanocomposite also confirms the higher absorption of the solar light and better separation of the e^-/h^+ pairs. There are several possibilities for electron transfer at the Ag-rGO@ZnO$_{NR}$ interface. The major possibility is the transfer of the photogenerated e^- from the conduction band (CB) of ZnO$_{NR}$ to the Fermi state of the attached Ag. Another possibility is the transfer of e^- from Ag (excitation to the surface plasmon resonance) to the ZnO$_{NR}$ CB. These e^- may be further transferred to the rGO, or they directly react with the dissolved O_2 and generate $^{\cdot}O_2^-$. The holes in the valance band react with the H_2O molecules and produce ·OH radical. These $^{\cdot}O_2^-$ and $^{\cdot}OH$ radicals act as strong reducing and oxidizing agents and fragments 2-CP molecules into mineralized products. The proposed mechanism for 2-CP degradation is given below, while its schematic scheme is shown in Fig. 11.

$$\mathrm{Ag} - r\mathrm{GO@ZnO_{NR}} + \mathrm{h}\nu \rightarrow \mathrm{Ag} - r\mathrm{GO@ZnO_{NR}}(e^- + h^+) \tag{11}$$

$$\mathrm{Ag} + \mathrm{h}\nu \rightarrow \mathrm{Ag}(\mathrm{e}^-) \tag{12}$$

$$\mathrm{ZnO_{NR}} + \mathrm{h}\nu \rightarrow \mathrm{ZnO_{NR}}(\mathrm{e}^- + \mathrm{h}^+) \tag{13}$$

$$\mathrm{e}^- + \mathrm{O_2} \rightarrow {}^{\cdot}\mathrm{O_2^-} \tag{14}$$

$$\mathrm{h}^+ + \mathrm{H_2O} \rightarrow {}^{\cdot}\mathrm{OH} \tag{15}$$

$${}^{\cdot}\mathrm{O_2^-} + {}^{\cdot}\mathrm{OH} + 2 - \mathrm{CP} \rightarrow \text{mineralized products} \tag{16}$$

Reusability of Ag-rGO@ZnO$_{NR}$

The stability and reusability of catalyst are the most important factors for commercialization and large-scale applications. For the reusability tests, the used

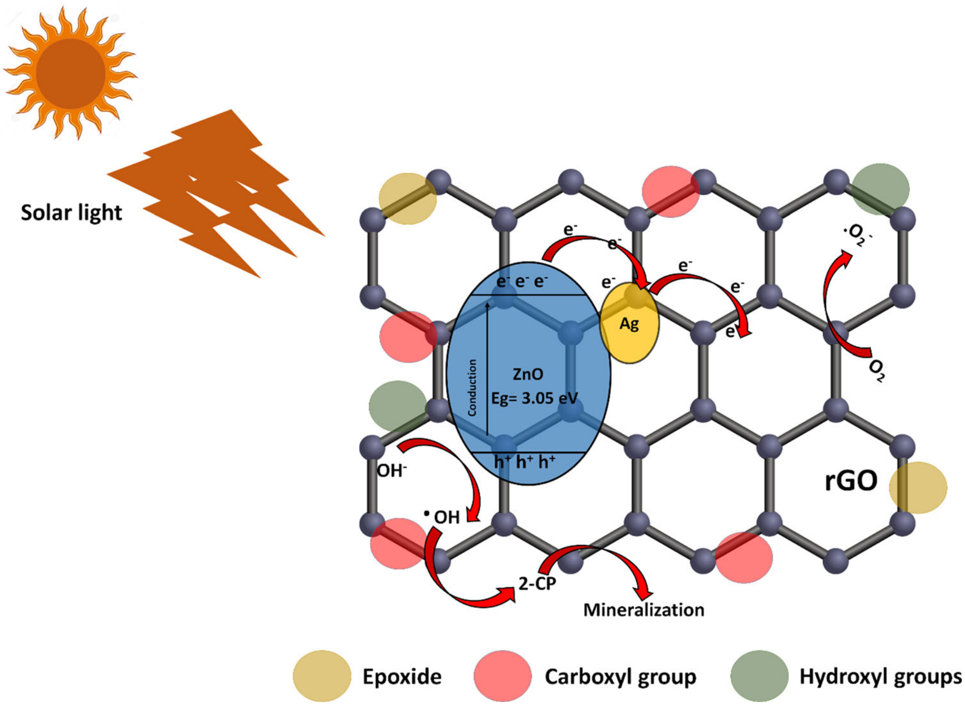

Figure 11 Proposed photocatalytic mechanism showing the formation of different possible heterojunctions in Ag-$\mathrm{rGO@ZnO_{NR}}$ and possible charge transfers for the degradation of 2-CP.

Ag-$\mathrm{rGO@ZnO_{NR}}$ nanocomposite was thoroughly washed with deionized water and subsequently dried, and the stability was investigated for three cycles (Fig. 10c). The efficiency of Ag-$\mathrm{rGO@ZnO_{NR}}$ remained 94% even after the three cycles. These results clearly indicate that the Ag-$\mathrm{rGO@ZnO_{NR}}$ nanocomposite is a stable catalyst and can be reused for multiple cycles.

Conclusion

In summary, the Ag-$\mathrm{rGO@ZnO_{NR}}$ were synthesized through facile *in situ* reduction of $AgNO_3$ onto $\mathrm{rGO@ZnO_{NR}}$ that showed almost complete degradation of 2-CP molecules with very high reusability of 94% under solar radiation. Moreover, the enhanced photocatalytic activity is attributed to the: added absorption of solar light of the higher wavelength and better separation of e^-/h^+ pairs due to the formation of heterojunctions between $\mathrm{ZnO_{NR}}$, rGO, and Ag. The Ag-$\mathrm{rGO@ZnO_{NR}}$ showed the lowest charge recombination rate in comparison to $\mathrm{ZnO_{NR}}$ and $\mathrm{rGO@ZnO_{NR}}$, which suggests its high photocatalytic efficiency. Structural analysis showed that Ag occupied the interstitial sites of $\mathrm{rGO@ZnO_{NR}}$ without changing the preferred orientations of the diffraction planes. The oxidation power of $\mathrm{ZnO_{NR}}$ decreased while the reduction strength became more negative with the addition of rGO and Ag, and the bandgap reduced from 3.05 ($\mathrm{ZnO_{NR}}$) to 2.87 eV (Ag-$\mathrm{rGO@ZnO_{NR)}}$. The functional groups of rGO were found to be responsible for the strong interaction with Zn, whereas Ag interacted with the diffused oxygen vacancies. In short, this study may provide a platform for understanding and further designing the ternary metal and metal oxide composites with graphene derivatives for the degradation of environmental pollutants.

Compliance with ethical standards

Conflict of interest There is no conflict of interest to declare.

References

[1] Kumar R, Laskar MA, Hewaidy IF, Barakat MA (2019) Modified adsorbents for removal of heavy metals from aqueous environment: a review. Earth Syst Environ 3:83–93. https://doi.org/10.1007/s41748-018-0085-3

[2] Rovira J, Domingo JL (2019) Human health risks due to exposure to inorganic and organic chemicals from textiles: a review. Environ Res 168:62–69. https://doi.org/10.1016/j.envres.2018.09.027

[3] Ali S, Rizwan M, Shakoor MB, Jilani A, Anjum R (2020) High sorption efficiency for As(III) and As(V) from aqueous solutions using novel almond shell biochar. Chemosphere 243:125330. https://doi.org/10.1016/j.chemosphere.2019.125330

[4] Ran X, Duan L, Chen X, Yang X (2018) Photocatalytic degradation of organic dyes by the conjugated polymer poly(1,3,4-oxadiazole)s and its photocatalytic mechanism. J Mater Sci 53:7048–7059. https://doi.org/10.1007/s10853-018-2025-x

[5] MalathiMadhavanAshokkumarArunachalam MJMP (2018) A review on BiVO4 photocatalyst: activity enhancement methods for solar photocatalytic applications. Appl Catal A 555:47–74. https://doi.org/10.1016/j.apcata.2018.02.010

[6] Bharath G, Anwer S, Mangalaraja RV, Alhseinat E, Banat F, Ponpandian N (2018) Sunlight-Induced photochemical synthesis of Au nanodots on α-Fe(2)O(3)@Reduced graphene oxide nanocomposite and their enhanced heterogeneous catalytic properties. Sci Rep 8:5718. https://doi.org/10.1038/s41598-018-24066-y

[7] Lu D, Zelekew OA, Abay AK, Huang Q, Chen X, Zheng Y (2019) Synthesis and photocatalytic activities of a CuO/TiO$_2$ composite catalyst using aquatic plants with accumulated copper as a template. RSC Adv 9:2018–2025. https://doi.org/10.1039/C8RA09645G

[8] Mudassir MA, Hussain SZ, Jilani A, Zhang H, Ansari TM, Hussain I (2019) Magnetic hierarchically macroporous emulsion-templated poly(acrylic acid)–iron oxide nanocomposite beads for water remediation. Langmuir 35:8996–9003. https://doi.org/10.1021/acs.langmuir.9b01121

[9] Ong CB, Ng LY, Mohammad AW (2018) A review of ZnO nanoparticles as solar photocatalysts: synthesis, mechanisms and applications. Renew Sust Energy Rev 81:536–551. https://doi.org/10.1016/j.rser.2017.08.020

[10] Schneider J, Matsuoka M, Takeuchi M et al (2014) Understanding TiO2 photocatalysis: mechanisms and materials. Chem Rev 114:9919–9986. https://doi.org/10.1021/cr5001892

[11] Jilani A, Othman MHD, Ansari MO et al (2019) Structural and optical characteristics, and bacterial decolonization studies on non-reactive RF sputtered Cu–ZnO@ graphene based nanoparticles thin films. J Mater Sci 54:6515–6529. https://doi.org/10.1007/s10853-019-03343-9

[12] Cao S, Wang H, Li H, Chen J, Zang Z (2020) Critical role of interface contact modulation in realizing low-temperature fabrication of efficient and stable CsPbIBr 2 perovskite solar cells. Chem Eng J 394:124903. https://doi.org/10.1016/j.cej.2020.124903

[13] Wang H, Cao S, Yang B et al (2020) NH4Cl-modified ZnO for high-performance CsPbIBr 2 Perovskite solar cells via low-temperature process. Solar RRL 4:1900363. https://doi.org/10.1002/solr.201900363

[14] Wang H, Zhang P, Zang Z (2020) High performance CsPbBr 3 quantum dots photodetectors by using zinc oxide nanorods arrays as an electron-transport layer. Appl Phys Lett 116:162103. https://doi.org/10.1063/5.0005464

[15] Zang Z (2018) Efficiency enhancement of ZnO/Cu$_2$O solar cells with well oriented and micrometer grain sized Cu$_2$O films. Appl Phys Lett 112:042106. https://doi.org/10.1063/1.5017002

[16] Mishra YK, Adelung R (2018) ZnO tetrapod materials for functional applications. Mater Today 21:631–651. https://doi.org/10.1016/j.mattod.2017.11.003

[17] Almoisheer N, Alseroury FA, Kumar R, Almeelbi T, Barakat MA (2019) Synthesis of graphene oxide/silica/carbon nanotubes composite for removal of dyes from wastewater. Earth Syst Environ 3:651–659. https://doi.org/10.1007/s41748-019-00109-w

[18] Putri LK, Ong W-J, Chang WS, Chai S-P (2015) Heteroatom doped graphene in photocatalysis: a review. Appl Surf Sci 358:2–14. https://doi.org/10.1016/j.apsusc.2015.08.177

[19] Rafique S, Roslan NA, Abdullah SM et al (2019) UV-ozone treated graphene oxide/ PEDOT:PSS bilayer as a novel hole transport layer in highly efficient and stable organic solar cells. Org Electron 66:32–42. https://doi.org/10.1016/j.orgel.2018.12.005

[20] Xue B, Zou Y (2018) High photocatalytic activity of ZnO–graphene composite. J Colloid Interface Sci 529:306–313. https://doi.org/10.1016/j.jcis.2018.04.040

[21] Raizada P, Sudhaik A, Singh P (2019) Photocatalytic water decontamination using graphene and ZnO coupled photocatalysts: a review. Mater Sci Energy Technol 2:509–525. https://doi.org/10.1016/j.mset.2019.04.007

[22] Prasad C, Tang H, Bahadur I (2019) Graphitic carbon nitride based ternary nanocomposites: from synthesis to their applications in photocatalysis—a recent review. J Mol Liq 281:634–654. https://doi.org/10.1016/j.molliq.2019.02.068

[23] Awazu K, Fujimaki M, Rockstuhl C et al (2008) A plasmonic photocatalyst consisting of silver nanoparticles embedded in titanium dioxide. J Am Chem Soc 130:1676–1680. https://doi.org/10.1021/ja076503n

[24] Chen X, Zheng Z, Ke X et al (2010) Supported silver nanoparticles as photocatalysts under ultraviolet and visible light irradiation. Green Chem 12:414–419. https://doi.org/10.1039/B921696K

[25] Hsueh Y-H, Hsieh C-T, Chiu S-T, Tsai P-H, Liu C-Y, Ke W-J (2019) Antibacterial property of composites of reduced graphene oxide with nano-silver and zinc oxide

nanoparticles synthesized using a microwave-assisted approach. Int J Mol Sci 20:5394. https://doi.org/10.3390/ijms20215394

[26] Meng A, Shao J, Fan X, Wang J, Li Z (2014) Rapid synthesis of a flower-like ZnO/rGO/Ag micro/nano-composite with enhanced photocatalytic performance by a one-step microwave method. RSC Adv 4:60300–60305. https://doi.org/10.1039/C4RA09695A

[27] Raj Pant H, Pant B, Joo Kim H et al (2013) A green and facile one-pot synthesis of Ag–ZnO/RGO nanocomposite with effective photocatalytic activity for removal of organic pollutants. Ceram Int 39:5083–5091. https://doi.org/10.1016/j.ceramint.2012.12.003

[28] Yokomizo Y, Krishnamurthy S, Kamat PV (2013) Photoinduced electron charge and discharge of graphene–ZnO nanoparticle assembly. Catal Today 199:36–41. https://doi.org/10.1016/j.cattod.2012.04.045

[29] Jilani A, Othman MHD, Ansari MO et al (2017) Facile spectroscopic approach to obtain the optoelectronic properties of few-layered graphene oxide thin films and their role in photocatalysis. New J Chem 41:14217–14227. https://doi.org/10.1039/C7NJ03614K

[30] Saini P, Sharma R, Chadha N (2017) Determination of defect density, crystallite size and number of graphene layers in graphene analogues using X-ray diffraction and Raman spectroscopy. Indian J Pure Appl Phys 55:625–629

[31] Mishra SK, Tripathi SN, Choudhary V, Gupta BD (2014) SPR based fibre optic ammonia gas sensor utilizing nanocomposite film of PMMA/reduced graphene oxide prepared by in situ polymerization. Sens Actuators B Chem 199:190–200. https://doi.org/10.1016/j.snb.2014.03.109

[32] Dehimi M, Touam T, Chelouche A et al (2015) Effects of low Ag doping on physical and optical waveguide properties of highly oriented Sol-Gel ZnO thin films. Adv Condens Matter Phys 2015:740208. https://doi.org/10.1155/2015/740208

[33] Basu S, Hazra SK (2017) Graphene-noble metal nanocomposites and applications for hydrogen sensors. C 3:29. https://doi.org/10.3390/c3040029

[34] Zeferino RS, Flores MB, Pal U (2011) Photoluminescence and Raman scattering in Ag-doped ZnO nanoparticles. J Appl Phys 109:014308. https://doi.org/10.1063/1.3530631

[35] Jilani A, Abdel-wahab MS, Al-ghamdi AA, Dahlan As, Yahia IS (2016) Nonlinear optical parameters of nanocrystalline AZO thin film measured at different substrate temperatures. Phys B 481:97–103. https://doi.org/10.1016/j.physb.2015.10.038

[36] Jilani A, Othman MHD, Ansari MO et al (2018) A simple route to layer-by-layer assembled few layered graphene oxide nanosheets: optical, dielectric and antibacterial aspects. J Mol Liq 253:284–296

[37] Gomathi M, Rajkumar PV, Prakasam A (2018) Study of dislocation density (defects such as Ag vacancies and interstitials) of silver nanoparticles, green-synthesized using Barleria cristata leaf extract and the impact of defects on the antibacterial activity. Results Phys 10:858–864. https://doi.org/10.1016/j.rinp.2018.08.011

[38] Thool GS, Singh AK, Singh RS, Gupta A, Susan MABH (2014) Facile synthesis of flat crystal ZnO thin films by solution growth method: a micro-structural investigation. J Saudi Chem Soc 18:712–721. https://doi.org/10.1016/j.jscs.2014.02.005

[39] Abdel-wahab MS, Jilani A, Yahia IS, Al-Ghamdi AA (2016) Enhanced the photocatalytic activity of Ni-doped ZnO thin films: morphological, optical and XPS analysis. Superlattices Microstruct 94:108–118. https://doi.org/10.1016/j.spmi.2016.03.043

[40] Lv W, Sun F, Tang D-M et al (2011) A sandwich structure of graphene and nickel oxide with excellent supercapacitive performance. J Mater Chem 21:9014–9019. https://doi.org/10.1039/C1JM10400D

[41] Yang Y, Rigdon W, Huang X, Li X (2013) Enhancing graphene reinforcing potential in composites by hydrogen passivation induced dispersion. Sci Rep 3:2086. https://doi.org/10.1038/srep02086

[42] Abid PS, Islam SS, Mishra P, Ahmad S (2018) Reduced graphene oxide (rGO) based wideband optical sensor and the role of temperature, defect states and quantum efficiency. Sci Rep 8:3537. https://doi.org/10.1038/s41598-018-21686-2

[43] Tai JY, Leong KH, Saravanan P, Sim LC (2018) E3S Web of conferences EDP sciences

[44] Kamarulzaman N, Kasim MF, Rusdi R (2015) Band gap narrowing and widening of ZnO nanostructures and doped materials. Nanoscale Res Lett 10:1034. https://doi.org/10.1186/s11671-015-1034-9

[45] Li J, Liu Y, Li H, Chen C (2016) Fabrication of g-C_3N_4/TiO_2 composite photocatalyst with extended absorption wavelength range and enhanced photocatalytic performance. J Photochem Photobiol A 317:151–160. https://doi.org/10.1016/j.jphotochem.2015.11.008

[46] Mousavi M, Habibi-Yangjeh A, Abitorabi M (2016) Fabrication of novel magnetically separable nanocomposites using graphitic carbon nitride, silver phosphate and silver chloride and their applications in photocatalytic removal of different pollutants using visible-light irradiation. J Colloid Interface Sci 480:218–231. https://doi.org/10.1016/j.jcis.2016.07.021

[47] Basu M, Garg N, Ganguli AK (2014) A type-II semiconductor (ZnO/CuS heterostructure) for visible light photocatalysis. J Mater Chem A 2:7517–7525. https://doi.org/10.1039/C3TA15446G

[48] Chen Y, Huang W, He D, Situ Y, Huang H (2014) Construction of heterostructured g-C_3N_4/Ag/TiO_2 microspheres with enhanced photocatalysis performance under visible-light irradiation. ACS Appl Mater Interfaces 6:14405–14414

[49] Kim Y, Kang S (2011) Effect of particle size on photoluminescence emission intensity in ZnO. Acta Mater 59:3024–3031. https://doi.org/10.1016/j.actamat.2011.01.042

[50] Liqiang J, Yichun Q, Baiqi W et al (2006) Review of photoluminescence performance of nano-sized semiconductor materials and its relationships with photocatalytic activity. Sol Energy Mater Sol Cells 90:1773–1787. https://doi.org/10.1016/j.solmat.2005.11.007

[51] Reddy G, Reddy J, Krishna RH, Gopal G (2017) Luminescence and spectroscopic investigations on Gd 3+ doped ZnO nanophosphor. J Asian Ceram Soc. https://doi.org/10.1016/j.jascer.2017.06.008

[52] Zhang X, Zhao Z, Zhang W et al (2016) Surface Defects Enhanced Visible Light Photocatalytic H2 Production for Zn-Cd-S Solid Solution. Small 12:793–801. https://doi.org/10.1002/smll.201503067

[53] Choudhury B, Dey M, Choudhury A (2014) Shallow and deep trap emission and luminescence quenching of TiO_2 nanoparticles on Cu doping. Appl Nanosci 4:499–506. https://doi.org/10.1007/s13204-013-0226-9

[54] Alberto M, Luque-Alled JM, Gao L et al (2017) Enhanced organophilic separations with mixed matrix membranes of polymers of intrinsic microporosity and graphene-like fillers. J Membr Sci 526:437–449. https://doi.org/10.1016/j.memsci.2016.12.061

[55] Wang DH, Hu Y, Zhao JJ, Zeng LL, Tao XM, Chen W (2014) Holey reduced graphene oxide nanosheets for high performance room temperature gas sensing. J Mater Chem A 2:17415–17420. https://doi.org/10.1039/C4TA03740E

[56] Choi YR, Yoon Y-G, Choi KS et al (2015) Role of oxygen functional groups in graphene oxide for reversible room-temperature NO_2 sensing. Carbon 91:178–187. https://doi.org/10.1016/j.carbon.2015.04.082

[57] Spilarewicz-Stanek K, Kisielewska A, Ginter J, Bałuszyńska K, Piwoński I (2016) Elucidation of the function of oxygen moieties on graphene oxide and reduced graphene oxide in the nucleation and growth of silver nanoparticles. RSC Adv 6:60056–60067. https://doi.org/10.1039/C6RA10483E

[58] John F, William F, Peter E, Kenneth D (1995) Handbook of X-ray photoelectron spectroscopy. Physical Electronics. Inc., Minnesota

[59] Tay YY, Li S, Sun CQ, Chen P (2006) Size dependence of Zn 2p 3/2 binding energy in nanocrystalline ZnO. Appl Phys Lett 88:173118. https://doi.org/10.1063/1.2198821

[60] Chang J, Ahmad MZ, Wlodarski W, Waclawik ER (2013) Self-assembled 3D ZnO porous structures with exposed reactive 0001 facets and their enhanced gas sensitivity. Sensors 13:8445–8460

[61] Kayaci F, Vempati S, Ozgit-Akgun C, Biyikli N, Uyar T (2014) Enhanced photocatalytic activity of homoassembled ZnO nanostructures on electrospun polymeric nanofibers: a combination of atomic layer deposition and hydrothermal growth. Appl Catal B 156–157:173–183. https://doi.org/10.1016/j.apcatb.2014.03.004

[62] Compton OC, Nguyen ST (2010) Graphene oxide, highly reduced graphene oxide, and graphene: versatile building blocks for carbon-based materials. Small 6:711–723. https://doi.org/10.1002/smll.200901934

[63] Yan Y, Al-Jassim MM, Wei S-H (2005) Oxygen-vacancy mediated adsorption and reactions of molecular oxygen on the ZnO $(10\bar{1}0)$ surface. Phys Rev B 72:161307. https://doi.org/10.1103/PhysRevB.72.161307

[64] Ziashahabi A, Prato M, Dang Z, Poursalehi R, Naseri N (2019) The effect of silver oxidation on the photocatalytic activity of Ag/ZnO hybrid plasmonic/metal-oxide nanostructures under visible light and in the dark. Sci Rep 9:11839. https://doi.org/10.1038/s41598-019-48075-7

[65] Ahmad M, Ahmad I, Ahmed E, Akhtar MS, Khalid NR (2020) Facile and inexpensive synthesis of Ag doped ZnO/CNTs composite: study on the efficient photocatalytic activity and photocatalytic mechanism. J Mol Liq 311:113326. https://doi.org/10.1016/j.molliq.2020.113326

[66] Yoo D-H, Cuong TV, Luan VH et al (2012) Photocatalytic performance of a Ag/ZnO/CCG multidimensional heterostructure prepared by a solution-based method. J Phys Chem C 116:7180–7184. https://doi.org/10.1021/jp210216w

[67] Mitra M, Ghosh A, Mondal A, Kargupta K, Ganguly S, Banerjee D (2017) Facile synthesis of aluminium doped zinc oxide-polyaniline hybrids for photoluminescence and enhanced visible-light assisted photo-degradation of organic contaminants. Appl Surf Sci 402:418–428. https://doi.org/10.1016/j.apsusc.2017.01.072

[68] Singh J, Satpati B, Mohapatra S (2017) Structural, optical and plasmonic properties of Ag-TiO2 hybrid plasmonic nanostructures with enhanced photocatalytic activity. Plasmonics 12:877–888. https://doi.org/10.1007/s11468-016-0339-6